Supplement of Atmos. Chem. Phys., 26, 4131–4152, 2026
https://doi.org/10.5194/acp-26-4131-2026-supplement

Atmospheric Chemistry and Physics
Open Access
EGU

Supplement of

Measurement report: Formation and brownness of aqueous secondary organic aerosol from the aged biomass-burning emissions in the Sichuan Basin, China

Chao Peng et al.

Correspondence to: Chao Peng (pengchao0623@sina.com) and Chongzhi Zhai (czz66818@sina.com)

S1. Source Apportionment of OA

Here, the positive matrix factorization (PMF) and multilinear engine (ME2) were implemented on the OA data measured by ToF-ACSM to determine the numbers and types of OA source factors (Paatero 1999; Paatero and Tapper 1994). The data analyses were conducted using the source finder (SoFi, Canonaco et al., 2013) tool version 6.3 for Igor Pro. PMF is a bilinear unmixing model that can describe the variability of a multivariate database as a linear combination of static factor profiles and their corresponding time series, as expressed in Eq. (S1):

$$X = GF + E \quad \text{(S1)}$$

where X refers to the measured OA mass spectral matrix containing i rows and j columns, F contains the factor profiles, G their corresponding time series, and E is the model residuals and the scaled residuals are minimized. The model uses a least-squares method to iteratively minimize the object function Q, defined as the sum of the squared residuals (e_{ij}) weighted by their respective uncertainties (σ_{ij}):

$$Q = \sum_{i=1}^{m} \sum_{j=1}^{n} \left(\frac{e_{ij}}{\sigma_{ij}}\right)^2 \quad \text{(S2)}$$

The PMF analysis was performed using the ME2, which allows for a comprehensive exploration of rotational ambiguity in the solution space (Canonaco et al., 2013). ME2 is used to introduce a priori information as an additional model input, constraining one or more factor profiles to a predetermined range (*a* value):

$$f_{j,solution} = f_j \pm a \times f_j \quad \text{(S3)}$$

where f refers to a row of the matrix F, j indicates the m/z of the ions, and the *a* value (from 0 to 1 with a step of 0.1) determines the extent to which the output profiles can differ from the model inputs.

The optimal number was selected by the discrimination of the tracers and the spectrum pattern of each source. Hydrocarbon-like OA (HOA) was dominated by alkyl ions with prominent ion fragments at $C_nH^+_{2n-1}$ and $C_nH^+_{2n+1}$ (m/z 41, 43, 55, 57, 69, 71, 83, and 85) in the spectra (Elser et al., 2016). Biomass-burning OA (BBOA) was identified by significant contributions from m/z 60 (mainly $C_2H_4O_2^+$) and m/z 73 (mainly $C_3H_5O_2^+$), they were the fragments of levoglucosan and mannosan emitted from incomplete biomass burning (Alfarra et al., 2007). Coal-combustion OA (CCOA) was characterized by unsaturated hydrocarbon ion fragments such as PAH-related ion fragments (i.e., m/z 77, 91, and 115) (Sun et al., 2016). Oxygenated OA (OOA) was distinguished by the prominent signal of m/z 43 (mainly $C_2H_3O^+$) and m/z 44 (mainly

CO_2^+) (Ng et al., 2011). Aqueous-phase oxidized OA (aqSOA) also had high correlation with m/z 43 and m/z 44, while it might show a significantly higher m/z 29 (mainly CHO^+) signal than other OA factors (Zhao et al., 2019; Zhong et al., 2021).

In this study, we performed the free PMF runs from 3 to 6 factors. The discrete spectra were more likely to reasonable results when N = 4, 5, and 6 (Fig. S4−S6). When N = 4, OOA1, OOA2, HOA and BBOA+CCOA were resolved. In BBOA+CCOA, the signals of levoglucosan (m/z 60) and PAH-related (m/z 91 and 115) ion fragments were obvious in the spectrum, suggesting BBOA was mixed with CCOA. In the N = 5 solutions, BBOA, CCOA, HOA, OOA, and aqSOA were resolved. These solutions were more reasonable than the N = 4 solutions because of the high relative humidity conditions during the sampling period. However, both CCOA and HOA exhibited significant signals at m/z 60, suggesting potential mixing with BBOA. When N = 6, the resolved OOA profiles were less evident than those in N = 5. Additionally, $Q/Q_{expected}$ showed that the solution with 5 factors was the most interpretable results (Fig. S7).

It should be noted that there was still a mix among POA factors in the five factors PMF solutions (Fig. S5). Initially, we tried to constrain COA by using COA profile in ME2 to identify if COA factor could be resolved from the OA sources. The COA was tried to constrain by using the profile from Elser et al. (2016). The restriction method ME2 was used to minimize PMF rotational ambiguity by the *a*-values from 0 to 1 with a step of 0.1 based on the reasonable result of PMF solutions. However, a large amount of blank values were shown, indicating COA was absent during the campaign. Then, all the combinations (BBOA and HOA, BBOA and CCOA, HOA and CCOA) were freely optimized by 11 *a*-values variables, respectively.

Here, BBOA was constrained by using the BBOA profile of Zhong et al. (2020), which was a clean BBOA profile from free PMF result. HOA and CCOA were constrained by using the HOA profile of Ng et al. (2011) and CCOA profile of Wang et al. (2017) to avoid mix with BBOA, respectively. Compared with previous research (Zhong et al., 2021), the optimal *a*-values solutions and ion fragments tracers were used to optimize the results, achieving effective minimization of m/z 60 signals in both HOA and CCOA profiles. In order to minimize the mix of BBOA from HOA and CCOA, a threshold of m/z 60 (the major ion tracer of BBOA) for the maximal fractional contribution was set as 0.006 (mean + 2σ) for HOA and CCOA,

respectively (Ng et al., 2011; Wang et al., 2017).

(1) When BBOA and HOA were freely combined in increments of 0.1 (from 0 to 1), the fractional contribution of m/z 60 in HOA ranged from 0.0017 to 0.0189. When the *a*-values of BBOA and HOA were set to ranges of 0−1 and 0−0.6, respectively, the fractional contribution of m/z 60 in HOA remained below 0.006. However, when the *a*-values of HOA extended to 0.7−1, the corresponding m/z 60 fractional contributions exceeded 0.006 (Fig. S8a). Therefore, only solutions with HOA *a*-values below 0.7 were retained, while all BBOA solutions with *a*-values ranging from 0 to 1 were retained.

(2) BBOA and CCOA were also freely combined by 11 *a*-values variables according to the *a*-values method in (1). When the *a*-values of CCOA were higher than 0.9, all fractional contributions of m/z 60 in CCOA were above 0.006 (Fig. S8b). In contrast, at CCOA *a*-values below 0.9, all the corresponding m/z 60 contributions in CCOA remained below this threshold (< 0.006). Therefore, the BBOA solutions with *a*-values ranging from 0 to 1 were retained, but all solutions with CCOA *a*-values exceeded 0.9 should be eliminated.

(3) After HOA and CCOA were constrained, the other unconstrained factors had a similar pattern with previously reported profiles. Based on the results from (1) and (2), we selected *a*-values ranges of 0−0.6 for HOA and 0−0.8 for CCOA for the factors combination. As shown in Fig. S8c, when the *a*-values of CCOA exceeded 0.7, most of the corresponding m/z 60 fractional contributions were above 0.006. Therefore, both the HOA and CCOA solutions with *a*-values from 0.7 to 1 were deleted based on the aforementioned criteria. Overall, 20 PMF solutions were retained and their average was used as the final result (Fig. S9).

S2. Estimation of Aerosol Liquid Water Content (ALWC)

The effect of inorganic ions on ALWC was estimated using a thermodynamic equilibrium model for the NH_4^+−SO_4^{2-}−NO_3^-−Cl^-−H_2O aerosol system, ISORROPIA-II (Fountoukis and Nenes, 2007). Here we ran the ISORROPIA II in forward mode, and the particles were assumed to be deliquescent, i.e., in metastable mode (Hennigan et al., 2015). The ammonium, nitrates, sulfates, and chlorides mass concentrations were measured by ToF-ACSM and the meteorological parameters (T and RH) were obtained from National Environmental Monitoring Station.

Meanwhile, the contribution of organics to ALWC was calculated by Zdanovskii−Stokes−Robinson (ZSR) mixing rule using the following equation (Guo et al., 2015; Huang et al., 2020; Nguyen et al., 2016; Xu et al., 2022):

$$W_{OA} = \frac{OA}{\rho_{OA}} \rho_w \frac{k_{OA}}{(100\%/a_w - 1)} \quad \text{(S4)}$$

where OA was the mass concentration of organics, ρ_w was the density of water (1.0 g cm^{-3}) and ρ_{OA} was the density of organics (1.4 g cm^{-3}) (Nguyen et al., 2016; Xu et al., 2022). k_{OA} was the hygroscopicity parameter of organic aerosol composition. We applied k_{OA} value of 0.08 for organic aerosols at urban site (Nguyen et al., 2016). a_w was the water activity (dimensionless). We assumed a_w was equivalent to RH for the sake of simplicity because of a lack of particle diameter data (Huang et al., 2020; Xu et al., 2022).

S3. Estimation of BC and BrC Absorption

Aerosol light absorption (Abs_λ) was caused by black carbon (BC) ($Abs_{\lambda,BC}$) and brown carbon (BrC) ($Abs_{\lambda,BrC}$). In this study, the Abs_λ value was measured in real time by AE33 (Magee Scientific) at seven wavelengths (i.e., 370, 470, 520, 590, 660, 880, and 950 nm) (Drinovec et al., 2015). Previous research indicated that Abs_λ measured by Aethalometer was influenced by the scattering effects of quartz filters and nonlinear loading effects (Coen et al., 2010). This study implemented real-time corrections for loading effects based on the parallel measurements of attenuation values (ATN1 and ATN2) from the AE33 (Drinovec et al., 2015):

$$\frac{Q_2}{Q_1} \times \mathrm{FVRF} = \frac{\ln(1-k \times \mathrm{ATN_2})}{\ln(1-k \times \mathrm{ATN_1})} \tag{S5}$$

$$k_{\mathrm{weighted}} = \frac{(\mathrm{ATN_{TA}} - \mathrm{ATN_1}) \times k_{\mathrm{old}} + (\mathrm{ATN_1} - \mathrm{ATN_{f2}}) \times k}{(\mathrm{ATN_{TA}} - \mathrm{ATN_{f2}})} \tag{S6}$$

$$\mathrm{Abs_\lambda} = \frac{A \times (\Delta \mathrm{ATN_{1,\lambda}}/100)}{Q_1 \times (1-\delta) \times C_\lambda \times (1 - k \times \mathrm{ATN_{1,\lambda}}) \times \Delta t} \tag{S7}$$

where A and Q are the spot size and flow rate onto which particles are collected over a certain time period (t), respectively; C_λ is factor to compensate for multiple scattering of the filter fibers. In this study, the scattering effects of quartz filters were modified automatically by a single C value of 2.14 for all wavelengths (Weingartner et al., 2003). The value of δ, the lateral airflow in the filter matrix under the optical chamber, is determined by measuring of input and output flow; the face velocity ratio factor (FVRF) is determined from the ATN_2/ATN_1 ratio obtained at low filter loadings (Drinovec et al., 2015). The parameter k is determined by numerically solving the Eq. (S5). ATN_{f2} and ATN_{TA} are the upper limit on the attenuation range and attenuation setting to trigger the tape advance (typically around 120 at 370 nm), respectively. A weighted value of the parameter k (k_{weighted}) is used for loading effect compensation. It should be noted that the different compensation algorithms might yield slightly different Abs_λ. However, the comparison of these approaches or the improvement of the compensation methodology used is beyond the scope of this study.

Using equations (S8) and (S9), BC concentrations and the coefficient k for eliminating filter scattering effects were calculated based on the measured ATN1 and ATN2 values, along with the mass concentrations of BC1 and BC2. The Abs_λ was derived from BC concentrations at different wavelengths and the mass absorption cross-section of aerosols (MAC_λ) according to equation (S10) (Zhu et al., 2017). Then, $Abs_{\lambda,BC}$ and $Abs_{\lambda,BrC}$ were calculated based on the equations (S11), (S12), and (S13)

(Qin et al., 2018; Wang et al., 2021; Zhu et al., 2017).

$$BC1 = BC \times (1 - k \times ATN1) \quad (S8)$$

$$BC2 = BC \times (1 - k \times ATN2) \quad (S9)$$

$$Abs_{\lambda} = BC_{\lambda} \times MAC_{\lambda} \quad (S10)$$

$$Abs_{BrC,\lambda 1} = Abs_{\lambda 1} - Abs_{BC,\lambda 1} \quad (S11)$$

$$Abs_{BC,\lambda 1} = Abs_{\lambda 2} \times (\lambda_2/\lambda_1)^{AAE_{BC}} \quad (S12)$$

$$AAE_{BC} = -\log_{10}(Abs_{880}/Abs_{950}) \div \log_{10}(880/950) \quad (S13)$$

where $Abs_{\lambda 2}$ represented the Abs at 880 nm. We assumed that Abs_{BrC} was considered negligible at 880 nm, and MAC_{λ} values were 18.47, 14.54, 13.14, 11.58, 10.35, 7.77, and 7.19 $m^2\ g^{-1}$ at 370, 470, 520, 590, 660, 880, and 950 nm, respectively (Drinovec et al., 2015; Qin et al., 2018; Zhu et al., 2017).

Previous research have demonstrated that AAE_{BC} is sensitive to the refractive index, size distribution, and coating of carbonaceous aerosols (Gyawali et al., 2009; Lack and Langridge, 2013; Li et al., 2019). In this study, the relative uncertainties of Abs_{BrC} and Abs_{BC} were estimated following the methodology described by Tian et al. (2019):

$$U_{Abs_{BC}}(\lambda) = \sqrt{(U_{Abs}(880\ nm))^2 + (AU_{AAE_{BC}} \times \ln(\frac{880}{\lambda}))^2} \quad (S14)$$

$$U_{Abs_{BrC}}(\lambda) = \frac{\sqrt{(U_{Abs}(\lambda) \times Abs(\lambda))^2 + (U_{Abs_{BC}}(\lambda) \times Abs_{BC}(\lambda))^2}}{Abs(\lambda) - Abs_{BC}(\lambda)} = \frac{\sqrt{(U_{Abs}(\lambda))^2 + (U_{Abs_{BC}}(\lambda) \times (1 - C_{BrC}(\lambda))^2}}{C_{BrC}(\lambda)} \quad (S15)$$

$$U_{C_{BrC}}(\lambda) = \sqrt{(U_{Abs}(\lambda))^2 + (U_{Abs_{BC}}(\lambda))^2} \quad (S16)$$

where $U_{Abs}(\lambda)$, $U_{Abs_{BC}}(\lambda)$, and $U_{Abs_{BrC}}(\lambda)$ represent the relative uncertainties of Abs, Abs_{BC}, and Abs_{BrC}, respectively. $AU_{AAE_{BC}}$ represents the absolute uncertainty of the $AAE_{BC} = -\log_{10}(Abs_{880}/Abs_{950}) \div \log_{10}(880/950)$, $\ln(880/\lambda)$ is used to adjust the $AU_{AAE_{BC}}$ to the relative uncertainty. Qin et al. (2018) fould AAE_{BC} ranges from 0.67 to 1.03 in core-shell scenarios with different refractive indexes, cited in this study. $U_{Abs}(\lambda)$ is specified as a constant value (± 5%) to represent uncertainty in the absorption measurements of the model AE33 at all the wavelengths (Tian et al., 2019; Titos et al., 2015). $C_{BrC}(\lambda)$ is the absorbance fraction of BrC relative to Abs.

The relative uncertainties of Abs_{BC} were estimated to be [−46%, +21%] at 370 nm, [−34%, +16%] at 470 nm, [−28%, +13%] at 520 nm, [−22%, +11%] at 590 nm,

[−16%, +8%] at 660 nm, and [−5%, +5%] at 880 nm. The relative uncertainty of Abs_{BrC}, as well as the relative uncertainties of C_{BrC}, can be calculated using equations (S15) and (S16), with a resulting uncertainty range of [−112%, +42%] at 370 nm.

$Abs_{\lambda,BrC}$ was caused by primary BrC ($Abs_{\lambda,BrC,pri}$) and secondary BrC ($Abs_{\lambda,BrC,sec}$). The $Abs_{\lambda,BrC,sec}$ value was estimated by a minimum R-squared (MRS) method at each wavelength developed from the BC-tracer method (Wang et al., 2019; Wu and Yu, 2016):

$$Abs_{\lambda,BrC} = Abs_{\lambda,BrC,pri} + Abs_{\lambda,BrC,sec} \quad (S17)$$

$$Abs_{\lambda,BrC,sec} = Abs_{\lambda,BrC} - \left(\frac{Abs_{\lambda,BrC}}{BC}\right)_{pri} \times BC \quad (S18)$$

where BC was the mass concentration (μg m^{-3}); $(Abs_{\lambda,BrC}/BC)_{pri}$ was the ratio of $Abs_{\lambda,BrC}$ to BC mass concentration in primary emissions (m^{-2} g^{-1}). The BC mass concentration and $Abs_{\lambda,BrC,sec}$ values caused by SOA were independent (Shrivastava et al., 2017).

Here, a series of arbitrary values for $(Abs_{\lambda,BrC}/BC)_{pri}$ from 0 to 40 in increments of 0.01 was used to calculate a set of $Abs_{\lambda,BrC,sec}$ values at each wavelength. A coefficient of determination (R^2) for the relationship between $Abs_{\lambda,BrC,sec}$ and BC mass concentration was derived. Detailed information on the method and validation of this approach could be found in Wu et al. (2024). Fig. S12 shows the series of R^2 values plotted against the assumed values of $(Abs_{\lambda,BrC}/BC)_{pri}$. As BC and $Abs_{BrC,sec,\lambda}$ were independent, the target value of $(Abs_{\lambda,BrC}/BC)_{pri}$ corresponded with the minimum R^2 ($Abs_{\lambda,BrC,sec}$, BC) was chosen to analyse at each wavelength. The bias of MRS result was < 23% when the measurement uncertainty was within 20% (Wu and Yu, 2016). The negative estimated $Abs_{BrC,sec,\lambda}$ values were set to zero, and the corresponding $Abs_{BrC,pri,\lambda}$ was taken as the observed $Abs_{BrC,\lambda}$.

S4. Assessment of a Multiple Linear Regression Method

In this study, the estimate of $Abs_{\lambda,BrC}$ for each OA component (Table S2), obtained through the multiple linear regression (MLR) method reconstruction, was evaluated by the normalized mean bias (NMB), root mean square error (RMSE), and index of agreement (IOA). These parameters were calculated as follows (Li et al., 2011):

$$NMB = \frac{\sum_{i=1}^{N}(P_i - O_i)}{\sum_{i=1}^{N} O_i} \quad (S19)$$

$$RMSE = \left[\frac{1}{N}\sum_{i=1}^{N}(C)^2\right]^{\frac{1}{2}} \quad (S20)$$

$$IOA = 1 - \frac{\sum_{i=1}^{N}(P_i - O_i)^2}{\sum_{i=1}^{N}(|P_i - \bar{O}| + |O_i - \bar{O}|)^2} \quad (S21)$$

where P_i and O_i were the $Abs_{\lambda,BrC}$ estimated by MLR method and measured by AE33, respectively; N was the total number of predictions used for comparison; $\bar{O}$ denoted the average of the observed $Abs_{\lambda,BrC}$. The IOA ranged from 0 to 1, with 1 indicating perfect agreement of $Abs_{\lambda,BrC}$ between the MLR reconstruction and AE33 measurement.

During the campaign, the NMB values of $Abs_{\lambda,BrC}$ were 11.8%, 32.0%, 26.6%, 25.3%, and 13.3% at 370, 470, 520, 590, and 660 nm, respectively. Meanwhile, the RMSE values of $Abs_{\lambda,BrC}$ were 13.5, 7.5, 4.7, 3.1, and 1.7 Mm^{-1}, respectively. The IOA values at each wavelength (0.99–1.00) were higher than 0.95. Additionally, as shown in Fig. S14, the $Abs_{\lambda,BrC}$ values estimated by MLR method showed the best correlations (r^2 = 0.86, 0.84, 0.78, 0.61, 0.54, respectively, $p < 0.001$) with those measured by AE33 at 370, 470, 520, 590, and 660 nm, respectively. The slopes of these relationships between $Abs_{\lambda,BrC}$ measured by AE33 and estimated by MLR method were 0.81, 0.96, 0.78, 0.61, and 0.54, respectively.

S5. Backward Trajectory Analysis

48-hr backward trajectories of air masses arriving at Yongchuan were calculated every hour with the starting height of 200 m above ground level by using the NOAA HYSPLIT model (http://ready.arl.noaa.gov/HYSPLIT_traj.php) (Stein et al., 2015). The trajectory cluster analysis was based on the GIS-based software TrajStat (Cabello et al., 2016; Wang et al., 2009). The fire spots were obtained from satellite observation (https://firms.modaps.eosdis.nasa.gov/active_fire/, last access: 28 August 2025).

Table S1. Summary of mass concentrations of OA (μg/m^3), the fraction of OA in fine particles ($PM_{2.5}$), and the fraction of BBOA in OA during the fall-winter period in different cities (based on hourly averaged data.)

Location (Season)	OA (μg m^{-3})	BBOA (μg m^{-3})	Fraction of OA in $PM_{2.5}$ (%)	Fraction of BBOA in OA (%)	References
Chongqing (Autumn)	24.1 ± 18.1	8.6 ± 7.7	46.6 ± 10.7	34.8 ± 11.2	This study
Chongqing (Winter)	16.4 ± 9.8	1.4 ± 0.9	48.8 ± 14.6	8.6 ± 5.0	(Tang et al., 2025)
Chongqing (Winter)	25.5 ± 11.8	4.7	49.0	15.6	(Zhang et al., 2023a)
Chengdu (Winter)	39.2 ± 3.9	8.9 ± 5.4	40.3 ± 7.6	22.7	(Bao et al., 2023)
Beijing (Winter)	22.1 ± 18.1	N.A.	34.2	N.A.	(Zhang et al., 2023b)
Shijiazhuang (Winter)	16.0 ± 9.7	N.A.	26.9	N.A.	(Zhang et al., 2023b)
Xi′an (Winter)	25.9 ± 18.0	N.A.	33.9	N.A.	(Zhang et al., 2023b)
Shanghai (Winter)	11.5	0.3	25.0	2.7	(Li et al., 2020)
Shanxi (Winter)	24.5 ± 21.1	2.8 ± 4.9	35.4	11.3	(Li et al., 2022)

Table S2. The Abs values and contributions of five OA factors to Abs_{BrC} at different wavelengths during the campaign.

OA factors	Parameter	370 nm	470 nm	520 nm	590 nm	660 nm
BBOA	Abs_{BBOA} (Mm^{-1})	19.4	6.0	3.8	2.2	1.2
	Contribution (%)	51.9	44.5	40.8	43.4	39.1
OOA	Abs_{OOA} (Mm^{-1})	4.1	2.1	1.5	0.8	0.5
	Contribution (%)	11.1	16.5	16.9	16.6	16.6
aqSOA	Abs_{aqSOA} (Mm^{-1})	6.2	2.3	1.6	0.9	0.7
	Contribution (%)	16.4	21.4	20.8	22.1	26.7
CCOA	Abs_{CCOA} (Mm^{-1})	4.3	1.0	0.7	0.4	0.2
	Contribution (%)	11.5	7.8	7.5	7.4	7.5
HOA	Abs_{HOA} (Mm^{-1})	3.4	1.3	1.3	0.5	0.3
	Contribution (%)	9.1	9.8	14.0	10.5	10.1

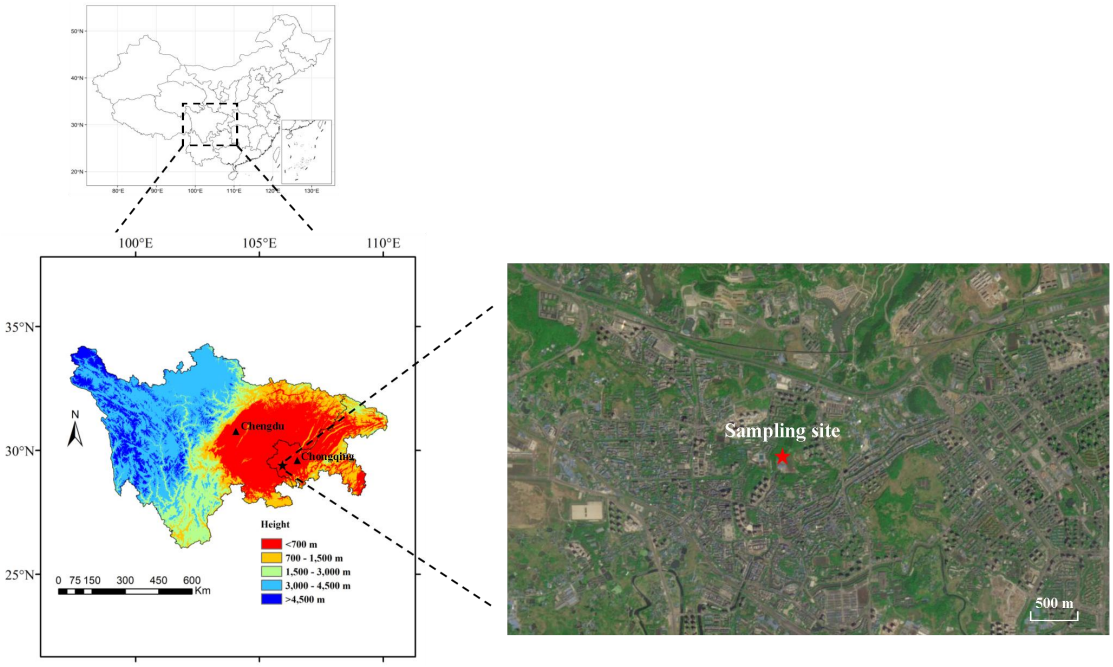

Figure S1. Location of the observation site in the Sichuan Basin (from Baidu Maps, © 2025 Baidu – GS(2023)3206).

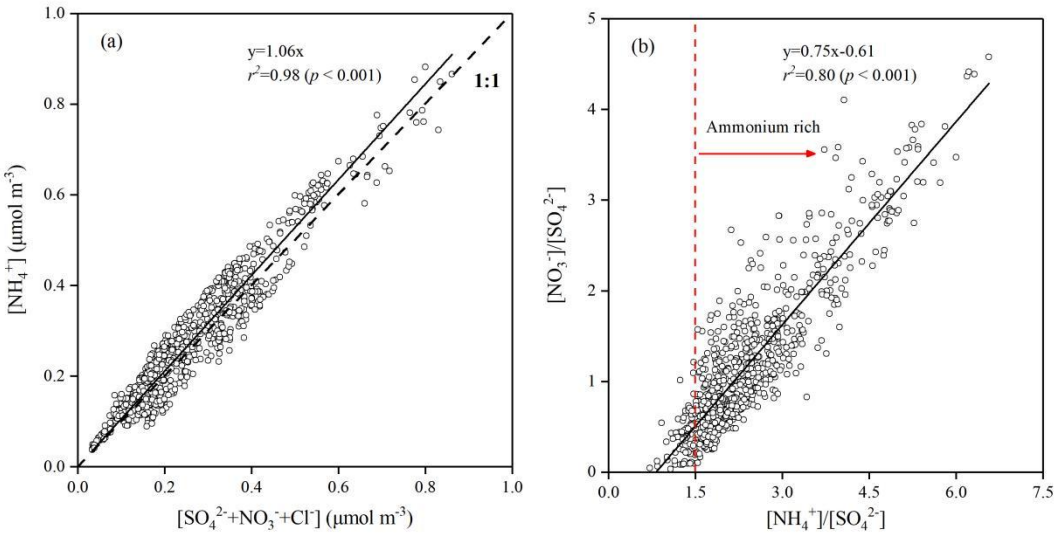

237

238 **Figure S2.** Scatter plots of **(a)** molar concentrations of NH_4^+ versus the sum of SO_4^{2-},

239 NO_3^-, and Cl^-, **(b)** molar ratios of NO_3^- to SO_4^{2-} versus NH_4^+ to SO_4^{2-}.

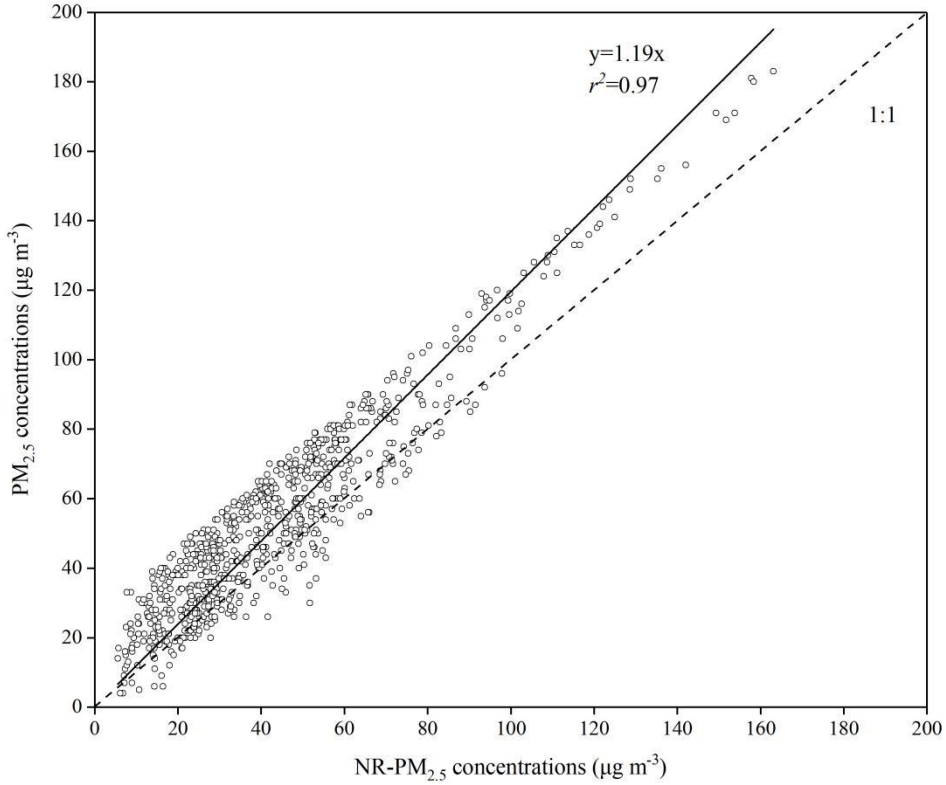

240

241 **Figure S3.** Scatter plot of $PM_{2.5}$ concentrations measured by a thermal analyzer
242 (5030i) versus those measured by ToF-ACSM.

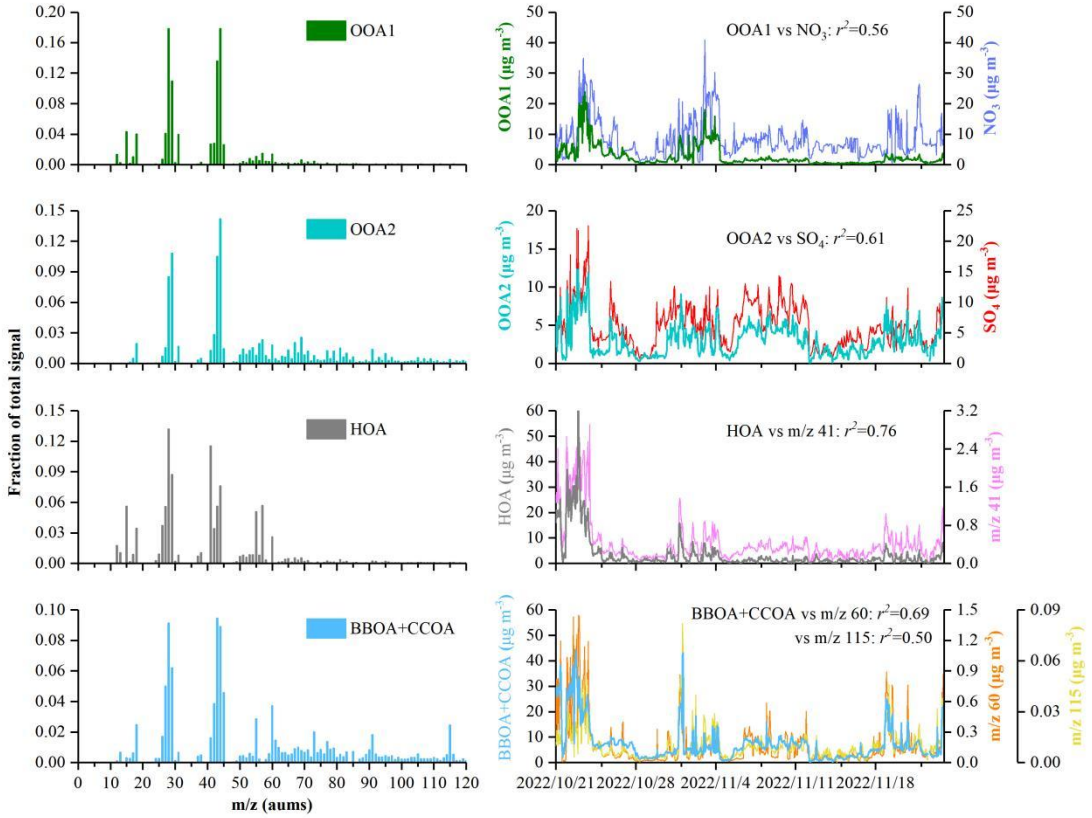

Figure S4. Mass spectra of four OA factors from free PMF result.

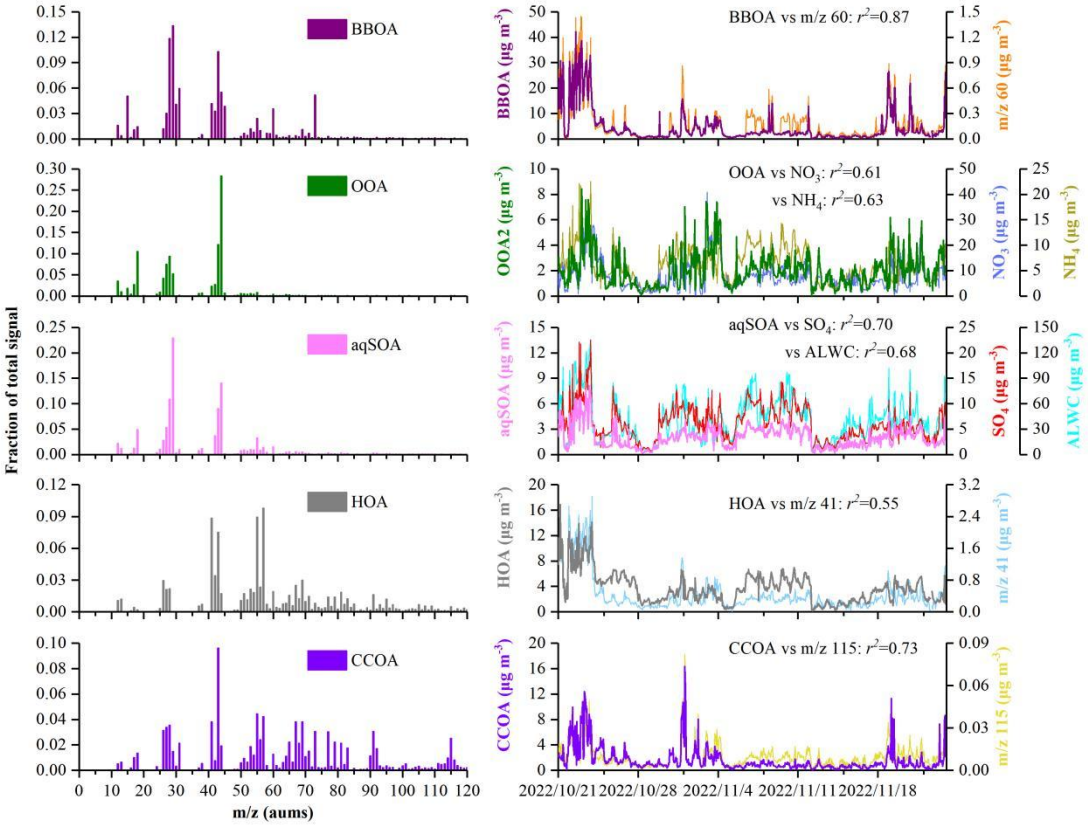

245

246 **Figure S5.** Mass spectra of five OA factors from free PMF result.

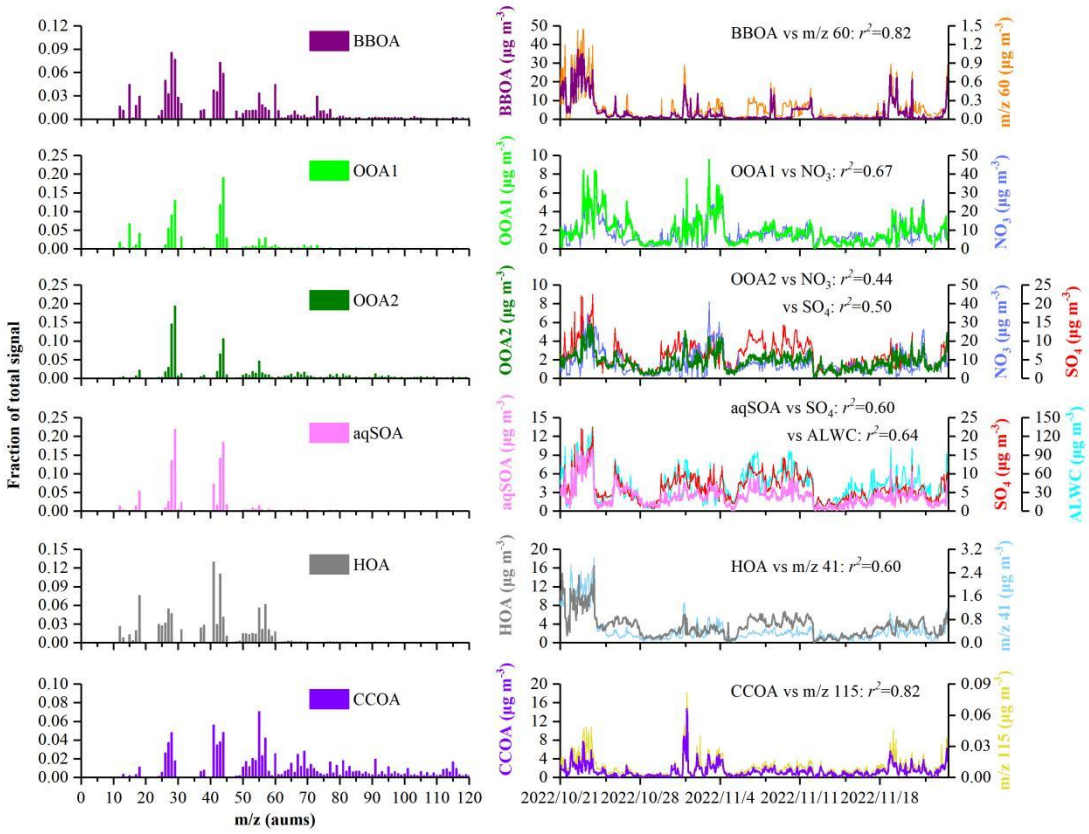

Figure S6. Mass spectra of six OA factors from free PMF result.

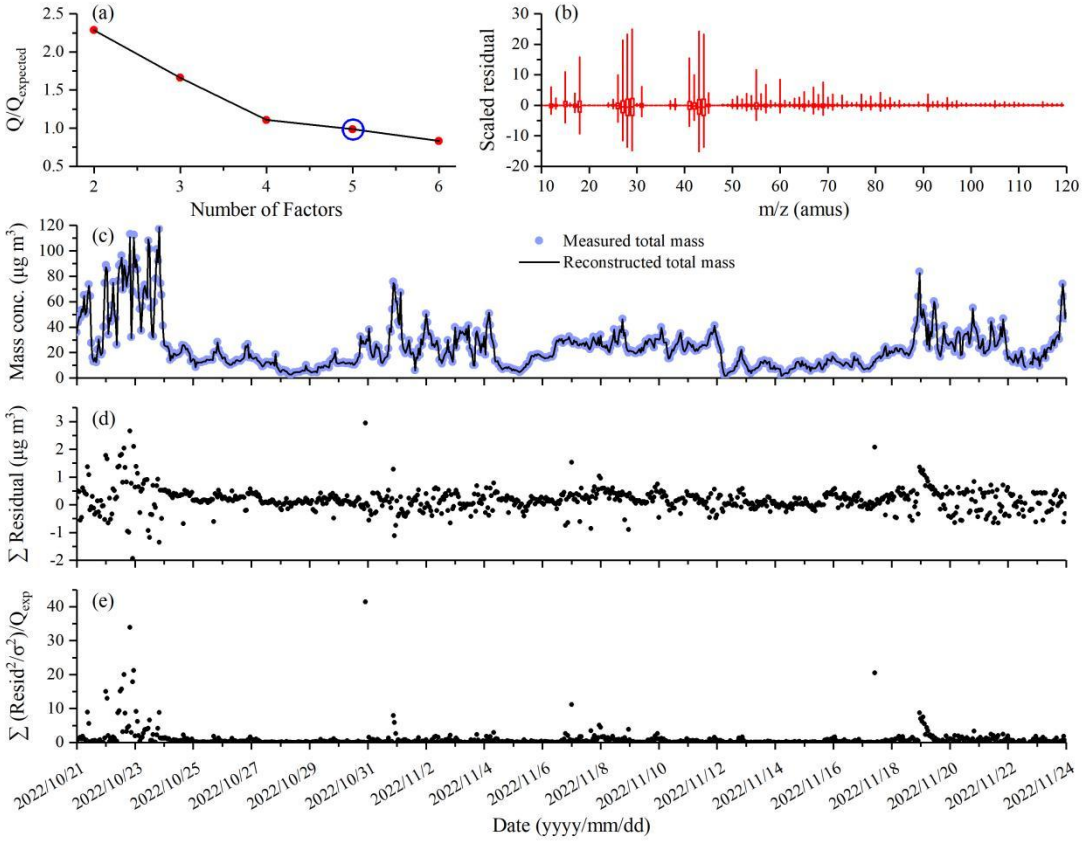

Figure S7. PMF diagnostic plots: **(a)** $Q/Q_{expected}$ varied as a function of the number of factors, **(b)** scaled residual for each m/z, **(c)** time series of measured and PMF reconstructed OA mass concentrations, **(d)** time series of residual, and (e) time series of $Q/Q_{expected}$.

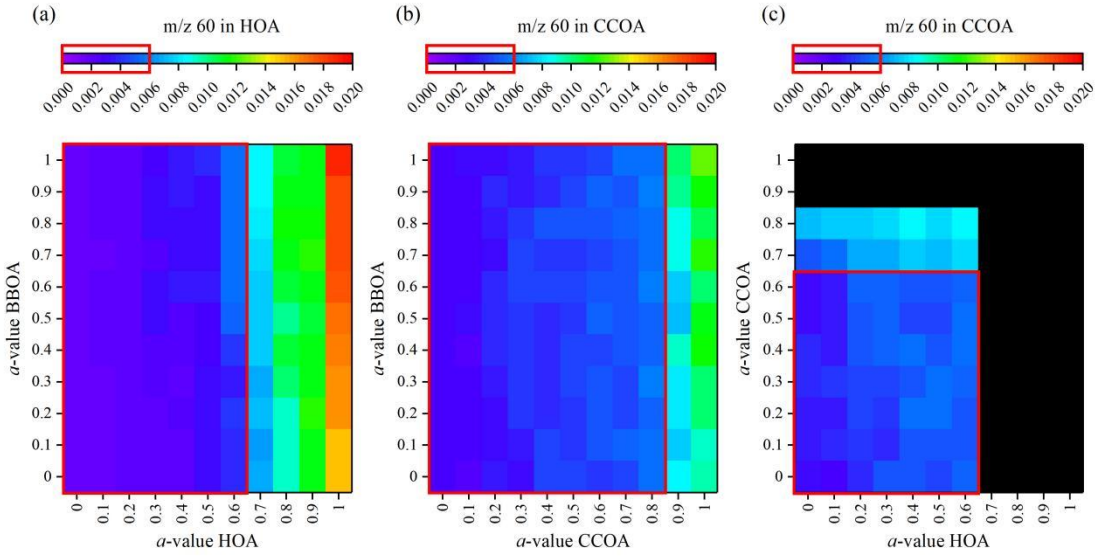

254

255 **Figure S8.** Relative contribution of m/z 60 in HOA and CCOA profiles over the
256 investigated *a*-values space; Acceptable contributions according to Ng et al. (2011)
257 and Wang et al. (2017) inside red area; Unselected *a*-values ranges for HOA (0.7−1)
258 and CCOA (0.9−1) for the factors combination (black area).

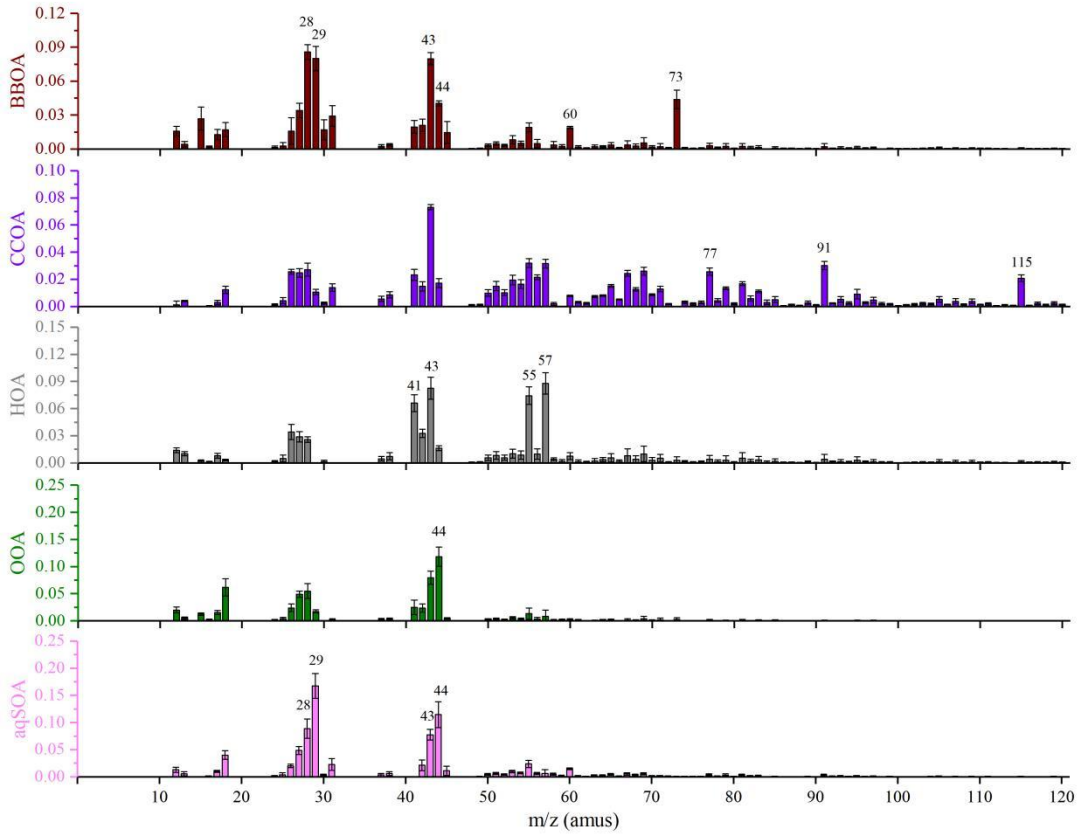

Figure S9. Mass spectra of five OA factors during the campaign.

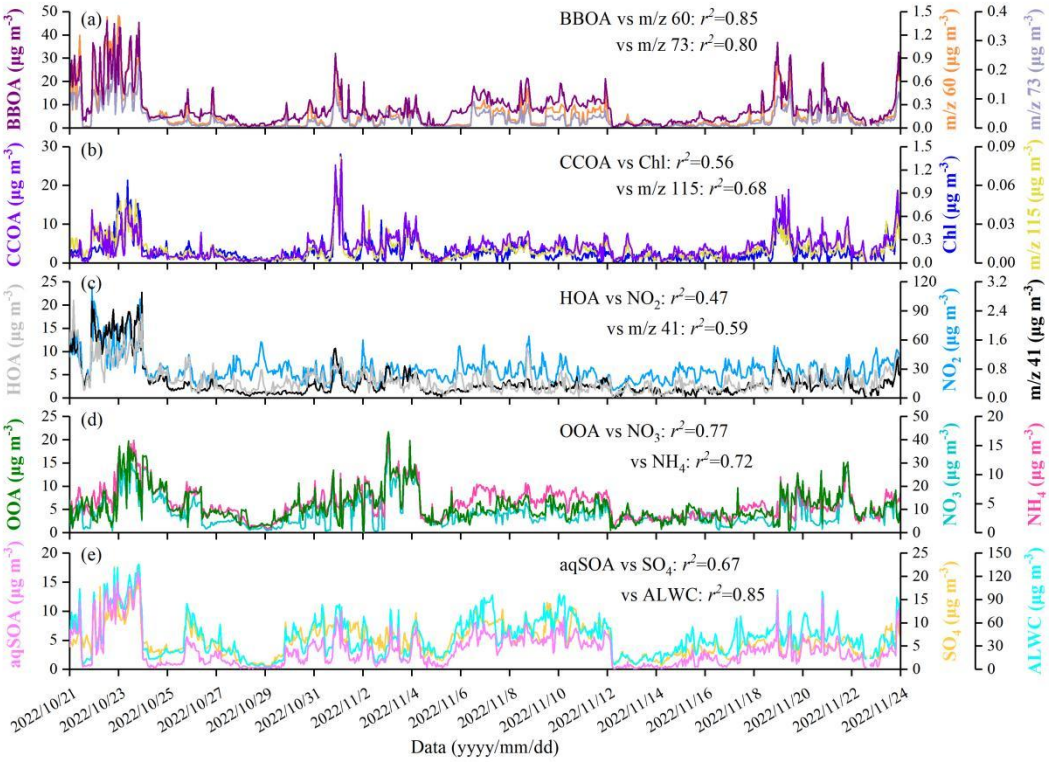

Figure S10. Time series of five OA factors and their corresponding tracer compounds.

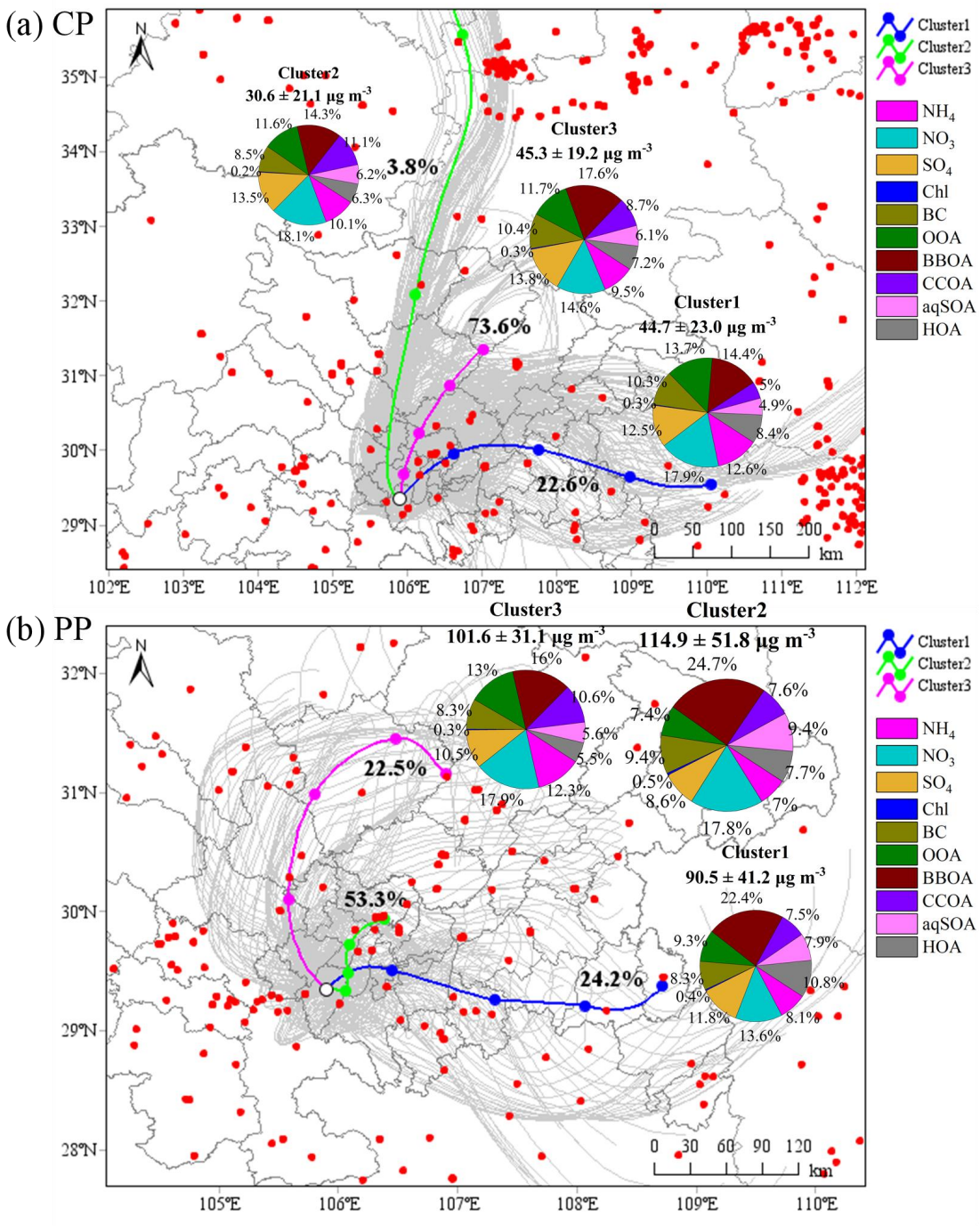

Figure S11. Backward trajectory clusters with corresponding wild fire spots distribution during **(a)** the clean period and **(b)** polluted period in Yongchuan. The blue, green, and purple lines represent the mean trajectories of cluster 1 to cluster 3, respectively. The pie charts show the contributions of different chemical compositions in BC+NR-$PM_{2.5}$ corresponding to each cluster.

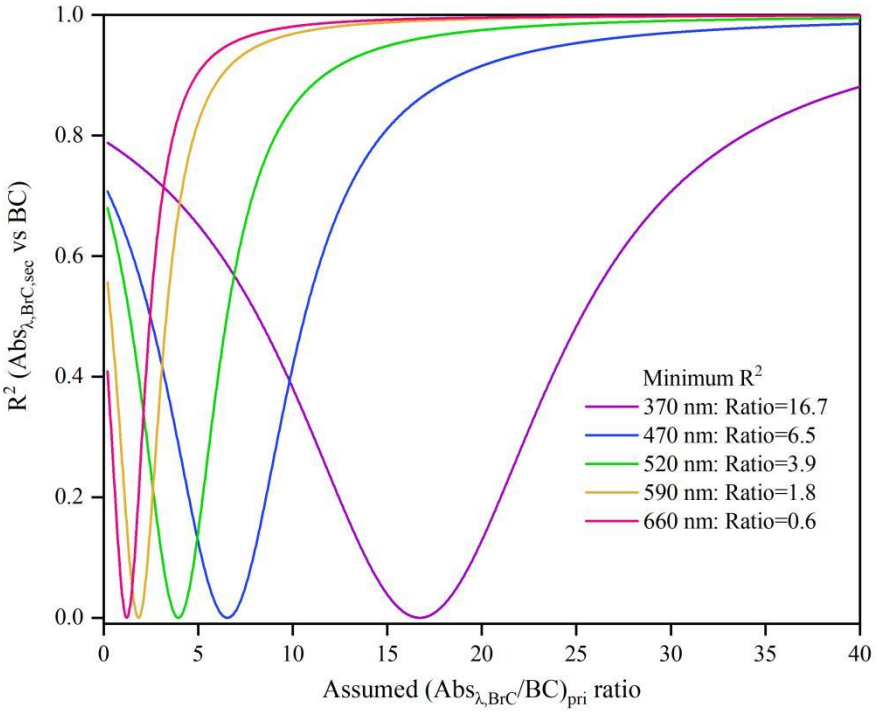

269

270 **Figure S12.** Coefficients of determination (R^2) for $Abs_{\lambda,BrC,sec}$ at 370, 470, 520, 590,
271 and 660 nm versus BC mass concentrations plotted against the assumed ratios of
272 $(Abs_{\lambda,BrC}/BC)_{pri}$.

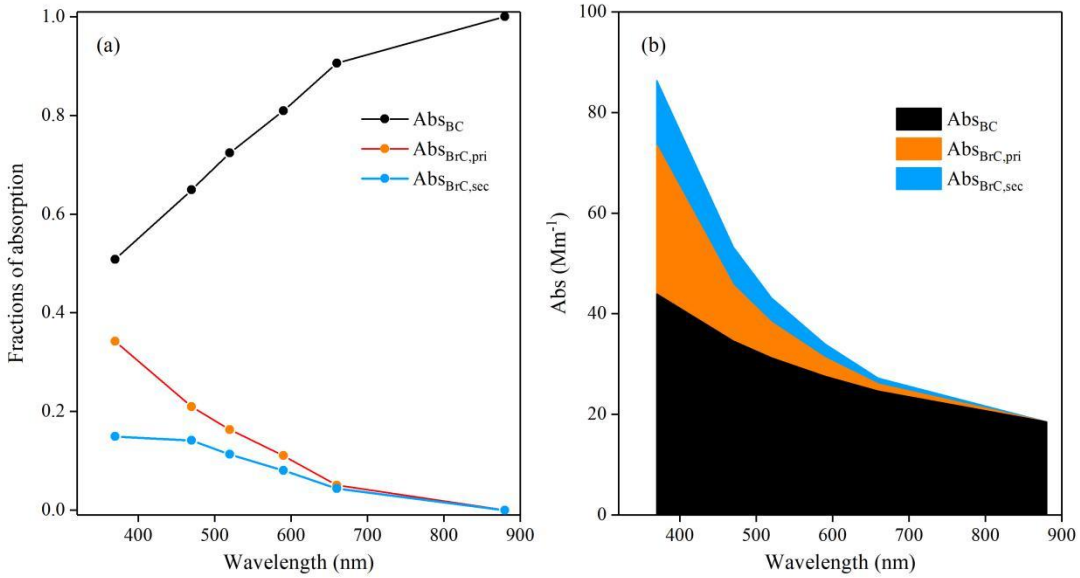

273

274 **Figure S13. (a)** Fractions and **(b)** contributions of Abs_{BC}, $Abs_{BrC,pri}$, and $Abs_{BrC,sec}$ to
275 Abs at different wavelengths from 370 to 880 nm during the campaign.

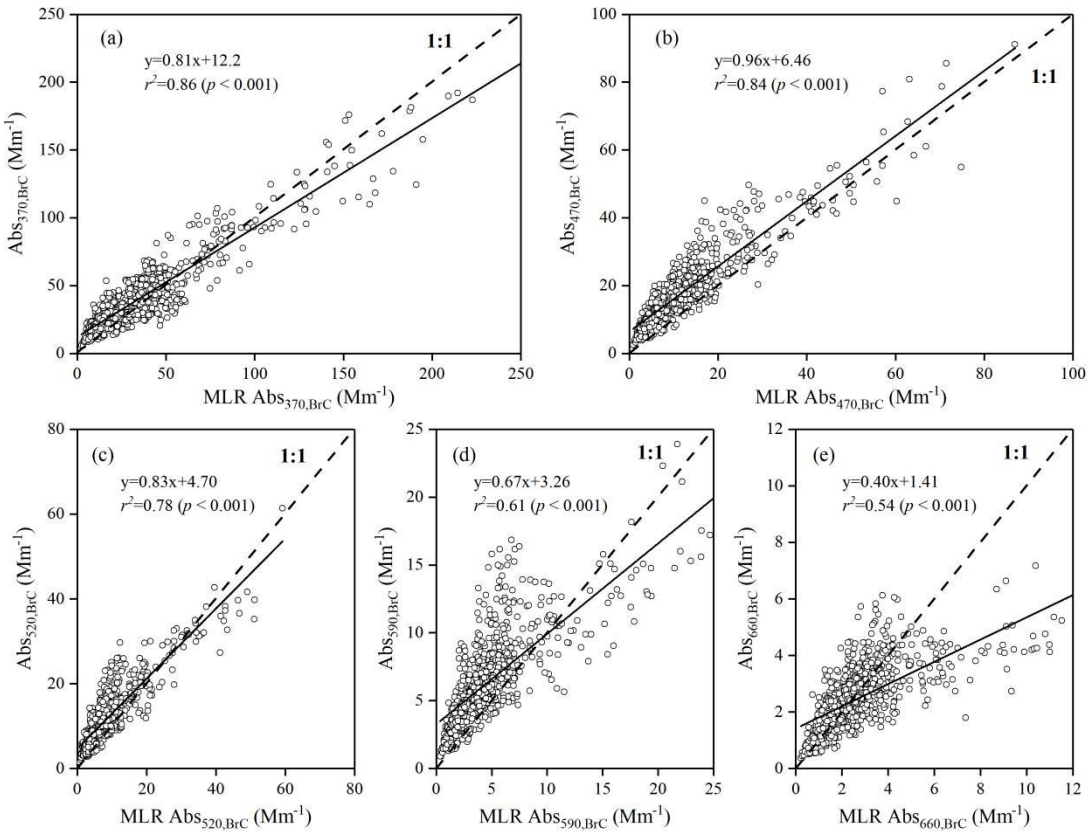

Figure S14. Scatter plots of $Abs_{370,BrC}$ at **(a)** 370, **(b)** 470, **(c)** 520, **(d)** 590, and **(e)** 660 nm measured by AE33 versus that obtained from a multiple linear regression (MLR) method.

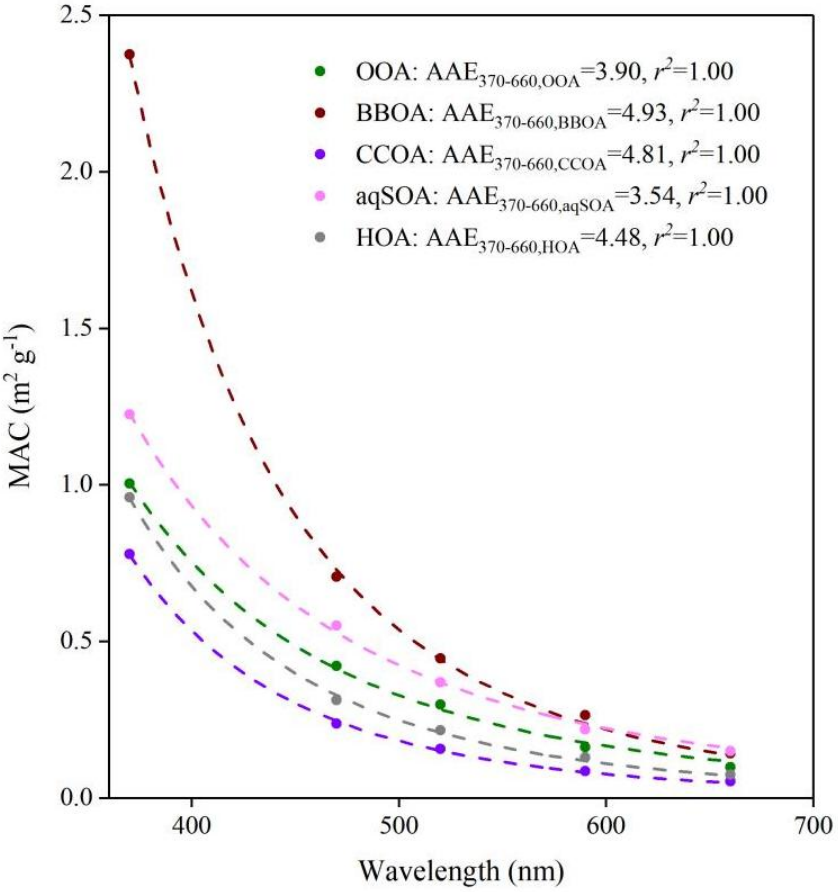

Figure S15. MAC of different OA factors as a function of wavelength from 370 to 660 nm.

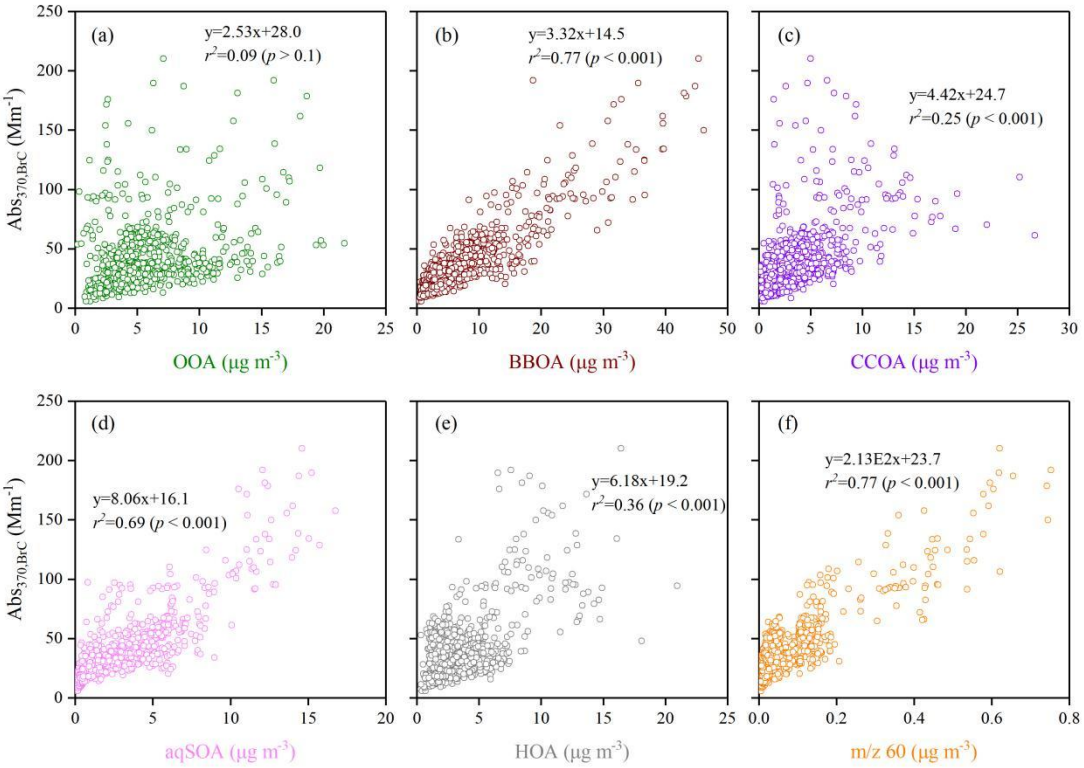

284

285 **Figure S16.** Correlation between $Abs_{370,BrC}$ and **(a)** OOA, **(b)** BBOA, **(c)** CCOA, **(d)**

286 aqSOA, **(e)** HOA, and **(f)** m/z 60 mass concentrations.

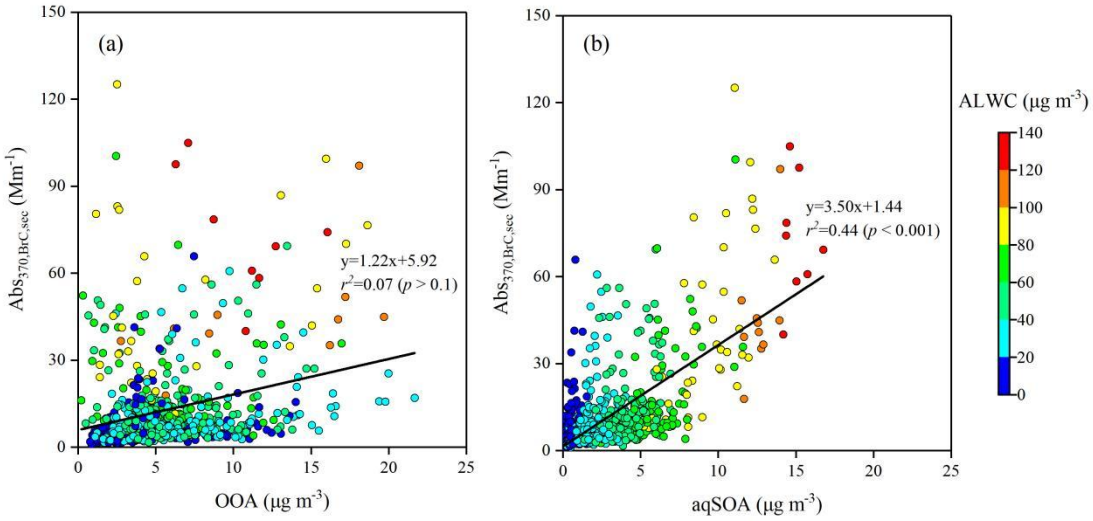

287

288 **Figure S17.** Scatter plots of $Abs_{370,BrC,sec}$ versus **(a)** OOA and **(b)** aqSOA mass
289 concentrations, coloured by ALWC.

References

Alfarra, M. R., Prévôt, A. S. H., Szidat, S., Sandradewi, J., Sandradewi, S., Lanz, V. A., Schreiber, D., Mohr, M., and Baltensperger, U.: Identification of the Mass Spectral Signature of Organic Aerosols from Wood Burning Emissions, Environ. Sci. Technol., 41, 5770−5777, https://doi.org/10.1021/es062289b, 2007.

Bao, Z. E., Zhang, X. Y., Li, Q., Zhou, J. W., Shi, G. M., Zhou, L., Yang, F. M., Xie, S. D., Zhang, D., Zhai, C. Z., Li, Z. L., Peng, C., and Chen, Y.: Measurement report: Intensive biomass burning emissions and rapid nitrate formation drive severe haze formation in the Sichuan Basin, China – insights from aerosol mass spectrometry, Atmos. Chem. Phys., 23, 1147−1167, https://doi.org/10.5194/acp-23-1147-2023, 2023.

Cabello, M., Orza, J. A. G., Dueñas, C., Liger, E., Gordo, E., and Cañete, S.: Back-trajectory analysis of African dust outbreaks at a coastal city in southern Spain: Selection of starting heights and assessment of African and concurrent Mediterranean contributions, Atmos. Environ., 140, 10−21, https://doi.org/10.1016/j.atmosenv.2016.05.047, 2016.

Canonaco, F., Crippa, M., Slowik, J. G., Baltensperger, U., and Prévôt, A. S. H.: SoFi, an IGOR-based interface for the efficient use of the generalized multilinear engine (ME-2) for the source apportionment: ME-2 application to aerosol mass spectrometer data, Atmos. Meas. Tech., 6, 3649−3661, https://doi.org/10.5194/amt-6-3649-2013, 2013.

Coen, M. C., Weingartner, E., Apituley, A., Ceburnis, D., Fierz-Schmidhauser, R., Flentje, H., Henzing, J. S., Jennings, S. G., Moerman, M., Petzold, A., Schmid, O., and Baltensperger, U.: Minimizing light absorption measurement artifacts of the Aethalometer: Evaluation of five correction algorithms, Atmos. Meas. Tech., 3, 457−474, https://doi.org/10.5194/amt-3-457-2010, 2010.

Drinovec, L., Močnik, G., Zotter, P., Prévôt, A. S. H., Ruckstuhl, C., Coz, E., Rupakheti, M., Sciare, J., Müller, T., Wiedensohler, A., and Hansen, A. D. A.: The "dual-spot" Aethalometer: an improved measurement of aerosol black carbon with real-time loading compensation, Atmos. Meas. Tech., 8, 1965−1979, https://doi.org/10.5194/amt-8-1965-2015, 2015.

Elser, M., Huang, R. J., Wolf, R., Slowik, J. G., Wang, Q. Y., Canonaco, F., Li, G. H., Bozzetti, C., Daellenbach, K. R., Huang, Y., Zhang, R. J., Li, Z. Q., Cao, J. J., Baltensperger, U., El-Haddad, I., and Prévôt, A. S. H.: New insights into $PM_{2.5}$

chemical composition and sources in two major cities in China during extreme haze events using aerosol mass spectrometry, Atmos. Chem. Phys., 16, 3207−3225, https://doi.org/10.5194/acp-16-3207-2016, 2016.

Fountoukis, C. and Nenes, A.: ISORROPIA II: a computationally efficient thermodynamic equilibrium model for K^+–Ca^{2+}–Mg^{2+}–NH_4^+–Na^+–SO_4^{2-}–NO_3^-–Cl^-–H_2O aerosols, Atmos. Chem. Phys., 7, 4639−4659, https://doi.org/10.5194/acp-7-4639-2007, 2007.

Guo, H. Y., Xu, L., Bougiatioti, A., Cerully, K. M., Capps, S. L., Hite Jr., J.R., Carlton, A. G., Lee, S. H., Bergin, M. H., Ng, N. L., Nenes, A., and Weber, R. J.: Fine-particle water and pH in the southeastern United States, Atmos. Chem. Phys., 15, 5211−5228, https://doi.org/10.5194/acp-15-5211-2015, 2015.

Gyawali, M., Arnott, W. P., Lewis, K., and Moosmüller, H.: In situ aerosol optics in Reno, NV, USA during and after the summer 2008 California wildfires and the influence of absorbing and non-absorbing organic coatings on spectral light absorption, Atmos. Chem. Phys., 9, 8007−8015, https://doi.org/10.5194/acp-9-8007-2009, 2009.

Hennigan, C. J., Izumi, J., Sullivan, A. P., Weber, R. J., and Nenes, A.: A critical evaluation of proxy methods used to estimate the acidity of atmospheric particles, Atmos. Chem. Phys., 15, 2775−2790, https://doi.org/10.5194/acp-15-2775-2015, 2015.

Huang, R. J., He, Y., Duan, J., Li, Y. J., Chen, Q., Zheng, Y., Chen, Y., Hu, W. W., Lin, C. S., Ni, H. Y., Dai, W. T., Cao, J. J., Wu, Y. F., Zhang, R. J., Xu, W., Ovadnevaite, J., Ceburnis, D., Hoffmann, T., and O'Dowd, C. D.: Contrasting sources and processes of particulate species in haze days with low and high relative humidity in wintertime Beijing, Atmos. Chem. Phys., 20, 9101−9114, https://doi.org/10.5194/acp-20-9101-2020, 2020.

Lack, D. A., and Langridge, J. M.: On the attribution of black and brown carbon light absorption using the Ångström exponent, Atmos. Chem. Phys., 13, 10535−10543, https://doi.org/10.5194/acp-13-10535-2013, 2013.

Li, G., Bei, N., Tie, X., and Molina, L. T.: Aerosol effects on the photochemistry in Mexico City during MCMA-2006/MILAGRO campaign, Atmos. Chem. Phys., 11, 5169−5182, https://doi.org/10.5194/acp-11-5169-2011, 2011.

Li, R., Wang, Q. Q., He, X., Zhu, S. H., Zhang, K., Duan, Y. S., Fu, Q. Y., Qiao, L. P., Wang, Y. J., Huang, L., Li, L., and Yu, J. Z.: Source apportionment of $PM_{2.5}$ in

Shanghai based on hourly organic molecular markers and other source tracers, Atmos. Chem. Phys., 20, 12047−12061, https://doi.org/10.5194/acp-20-12047-2020, 2020.

Li, Y., Du, A. D., Li, Z. J., Li, J., Chen, C., Sun, J. X., Qiu, Y. M., Zhang, Z. Q., Wang, Q. Q., Xu, W. Q., Liu, X. A., Ji, D. S., Zhang, W. J., Sun, Y. L.: Investigation of sources and formation mechanisms of fine particles and organic aerosols in cold season in Fenhe Plain, China, Atmos. Res., 268, 106018, https://doi.org/10.1016/j.atmosres.2022.106018, 2022.

Li, Z. J., Tan, H. B., Zheng, J., Liu, L., Qin, Y. M., Wang, N., Li, F., Li ,Y. J., Cai, M. F., Ma, Y., and Chan, C. K.: Light absorption properties and potential sources of particulate brown carbon in the Pearl River Delta region of China, Atmos. Chem. Phys., 19, 11669−11685, https://doi.org/10.5194/acp-19-11669-2019, 2019.

Ng, N. L., Canagaratna, M. R., Jimenez, J. L., Zhang, Q., Ulbrich, I. M., and Worsnop, D. R.: Real-Time Methods for Estimating Organic Component Mass Concentrations from Aerosol Mass Spectrometer Data, Environ. Sci. Technol., 45, 910−916, https://doi.org/10.1021/es102951k, 2011.

Nguyen, T. K. V., Zhang, Q., Jimenez, J. L., Pike, M., and Carlton, A. G.: Liquid Water: Ubiquitous Contributor to Aerosol Mass, Environ. Sci. Technol. Lett., 3, 257−263, https://doi.org/10.1021/acs.estlett.6b00167, 2016.

Paatero, P.: The Multilinear Engine: A Table-Driven, Least Squares Program for Solving Multilinear Problems, Including the n-Way Parallel Factor Analysis Model, J. Comput. Graph. Stat., 8, 854−888, https://doi.org/10.1080/10618600.1999.10474853, 1999.

Paatero, P. and Tapper, U.: Positive matrix factorization: A non-negative factor model with optimal utilization of error estimates of data values, Environmetrics, 5, 111−126, https://doi.org/10.1002/env.3170050203, 1994.

Qin, Y. M., Tan, H. B., Li, Y. J., Li, Z. J., Schurman, M. I., Liu, L., Wu, C., and Chan, C. K.: Chemical characteristics of brown carbon in atmospheric particles at a suburban site near Guangzhou, China, Atmos. Chem. Phys., 18, 16409−16418, https://doi.org/10.5194/acp-18-16409-2018, 2018.

Shrivastava, M., Cappa, C. D., Fan, J., Goldstein, A. H., Guenther, A. B., Jimenez, J. L., Kuang, C., Laskin, A., Martin, S. T., Ng, N. L., Petaja, T., Pierce, J. R., Rasch, P. J., Roldin, P., Seinfeld, J. H., Shilling, J., Smith, J. N., Thornton, J. A., Volkamer, R., Wang, J., Worsnop, D. R., Zaveri, R. A., Zelenyuk, A., and Zhang, Q.: Recent

advances in understanding secondary organic aerosol: Implications for global climate forcing, Rev. Geophys., 55, 509−559, https://doi.org/10.1002/2016RG000540, 2017.

Stein, A. F., Draxler, R. R., Rolph, G. D., Stunder, B. J. B., Cohen, M. D., and Ngan, F.: NOAA's HYSPLIT Atmospheric Transport and Dispersion Modeling System, American Meteorological Society, 96, 2059−2077, https://doi.org/10.1175/BAMS-D-14-00110.1, 2015.

Sun, Y. L., Du, W., Fu, P. Q., Wang, Q. Q., Li, J., Ge, X. L., Zhang, Q., Zhu, C. M., Ren, L. J., Xu, W. Q., Zhao, J., Han, T. T., Worsnop, D. R., and Wang, Z. F.: Primary and secondary aerosols in Beijing in winter: sources, variations and processes, Atmos. Chem. Phys., 16, 8309−8329, https://doi.org/10.5194/acp-16-8309-2016, 2016.

Tang, H. H., Li, Z. L., Tian, M., Peng, C., Ding, Y., Chen, M. L., Wang, X., C., Chen, Y., Yang, F. M., and Zhai, C. Z.: Formation of Oxidized Organic Aerosols in Winter Haze in a Megacity of Southwest China: Implication for the Importance of Biomass Burning, J. Geophys. Res. Atmos., 130, e2025JD044028, https://doi.org/10.1029/2025JD044028, 2025.

Tian, J., Wang, Q. Y., Ni, H. Y., Wang, M., Zhou, Y. Q., Han, Y. M., Shen, Z. X., Pongpiachan, S., Zhang, N. N., Zhao, Z. Z., Zhang, Q., Zhang, Y., Long, X., and Cao, J. J.: Emission Characteristics of Primary Brown Carbon Absorption From Biomass and Coal Burning: Development of an Optical Emission Inventory for China, J. Geophys. Res. Atmos., 124, 1879−1893, https://doi.org/10.1029/2018jd029352, 2019.

Titos, G., Lyamani, H., Drinovec, L., Olmo, F. J., Močnik, G., and Alados-Arboledas, L.: Evaluation of the impact of transportation changes on air quality, Atmos. Environ., 114, 19−31, https://doi.org/10.1016/j.atmosenv.2015.05.027, 2015.

Wang, J. F., Ye, J. H., Zhang, Q., Zhao, J., Wu, Y. Z., Li, J. Y., Liu, D. T., Li, W. J., Zhang, Y. G., Wu, C., Xie, C. H., Qin, Y. M., Lei, Y. L., Huang, X. P., Guo, J. P., Liu, P. F., Fu, P. Q., Li, Y. J., Lee, H. C., Choi, H., Zhang, J., Liao, H., Chen, M. D., Sun, Y. L., Ge, X. L., Martin, S. T., and Jacob, D. J.: Aqueous production of secondary organic aerosol from fossil-fuel emissions in winter Beijing haze, Proc. Natl. Acad. Sci. USA, 118, e2022179118, https://doi.org/10.1073/pnas.2022179118, 2021.

Wang, Q. Y., Ye, J. H., Wang, Y. C., Zhang, T., Ran, W. K., Wu, Y. F., Tian, J., Li, L.,

Zhou, Y. Q., Ho, H. S. S., Dang, B., Zhang, Q., Zhang, R. J., Chen, Y., Zhu, C. S., and Cao, J. J.: Wintertime Optical Properties of Primary and Secondary Brown Carbon at a Regional Site in the North China Plain, Environ. Sci. Technol., 53, 12389−12397, https://doi.org/10.1021/acs.est.9b03406, 2019.

Wang, Y. C., Huang, R. J., Ni, H. Y., Chen, Y., Wang, Q. Y., Li, G. H., Tie, X. X., Shen, Z. X., Huang, Y., Liu, S. X., Dong, W. M., Xue, P., Fröhlich, R., Canonaco, F., Elser, M., Daellenbach, K. R., Bozzetti, C., El Haddad, I., Prévôt, A. S. H., Canagaratna, M. R., Worsnop, D. R., and Cao, J. J.: Chemical composition, sources and secondary processes of aerosols in Baoji city of northwest China, Atmos. Environ., 158, 128−137, https://doi.org/10.1016/j.atmosenv.2017.03.026, 2017.

Wang, Y. Q., Zhang, X. Y., and Draxler, R. R.: TrajStat: GIS-based software that uses various trajectory statistical analysis methods to identify potential sources from long-term air pollution measurement data, Environ. Modell. Softw. 24, 938−939, https://doi.org/10.1016/j.envsoft.2009.01.004, 2009.

Weingartner, E., Saathoff, H., Schnaiter, M., Streit, N., Bitnar, B., and Baltensperger, U.: Absorption of light by soot particles: determination of the absorption coefficient by means of aethalometers, J. Aerosol Sci., 34, 1445−1463, doi:10.1016/s00218502(03)00359-8, 2003.

Wu, C. and Yu, J. Z.: Determination of primary combustion source organic carbon-to-elemental carbon (OC/EC) ratio using ambient OC and EC measurements: Secondary OC-EC correlation minimization method, Atmos. Chem. Phys., 16, 5453−5465, https://doi.org/10.5194/acp-16-5453-2016, 2016.

Wu, H., Peng, C., Zhai, T. Y., Deng, J. C., Lu, P. L., Li, Z. L., Chen, Y., Tian, M., Bao, Z. E., Long, X., Yang, F. M., and Zhai, C. Z.: Characteristics of light absorption and environmental effects of Brown carbon aerosol in Chongqing during summer and winter based on online measurement: Implications of secondary formation, Atmos. Environ., 338, 120843, https://doi.org/10.1016/j.atmosenv.2024.120843, 2024.

Xu, B. Q., Zhang, G., Gustafsson, Ö., Kawamura, K., Li, J., Andersson, A., Bikkina, S., Kunwar, B., Pokhrel, A., Zhong, G. C., Zhao, S. Z., Li, J., Huang, C., Cheng, Z. N., Zhu, S. Y., Peng, P. A., and Sheng, G. Y.: Large contribution of fossil-derived components to aqueous secondary organic aerosols in China, Nat. Commun., 13, 5115, https://doi.org/10.1038/s41467-022-32863-3, 2022.

Zhang, X. Y., Bao, Z. R., Zhang, L. Y., Zhou, J. W., Che, H. X., Li, Q., Tian, M., Yang,

F. M., and Chen, Y.: Biomass burning and aqueous reactions drive the elevation of wintertime $PM_{2.5}$ in the rural area of the Sichuan basin, China, Atmos. Environ., 306, 119779, https://doi.org/10.1016/j.atmosenv.2023.119779, 2023a.

Zhang, Y., Tian, J., Wang, Q. Y., Qi, L., Manousakas, M. I., Han, Y. M., Ran, W. K., Sun, Y. L., Liu, H. K., Zhang, R. J., Wu, Y. F., Cui, T. Q., Daellenbach, K. R., Slowik, J. G., Prévôt, A. S. H., and Cao, J. J.: High-time-resolution chemical composition and source apportionment of $PM_{2.5}$ in northern Chinese cities: implications for policy, Atmos. Chem. Phys., 23, 9455−9471, https://doi.org/10.5194/acp-23-9455-2023, 2023b.

Zhao, J., Qiu, Y. M.,Zhou, W., Xu, W. Q., Wang, J. F., Zhang, Y. J., Li, L. J., Xie, C. H., Wang, Q. Q., Du, W., Worsnop, D. R., Canagaratna, M. R., Zhou, L. B., Ge, X. L., Fu, P. Q., Li, J., Wang, Z. F., Donahue, N. M., and Sun, Y. L.: Organic Aerosol Processing During Winter Severe Haze Episodes in Beijing, J. Geophys. Res.: Atmos., 124, 10248−10263, https://doi.org/10.1029/2019JD030832, 2019.

Zhong, H. B., Huang, R. J., Chang, Y. H., Duan, J., Lin, C. S., and Chen, Y.: Enhanced formation of secondary organic aerosol from photochemical oxidation during the COVID-19 lockdown in a background site in Northwest China, Sci. Total Environ., 778, 144947, https://doi.org/10.1016/j.scitotenv.2021.144947, 2021.

Zhong, H. B., Huang, R. J., Duan, J., Lin, C. S., Gu, Y. F., Wang, Y., Li, Y. J., Zheng, Y., Chen, Q., Chen, Y., Dai, W. T., Ni, H. Y., Chang, Y. H., Worsnop, D. R., Xu, W., Ovadnevaite, J., Ceburnis, D., and O'Dowd, C. D.: Seasonal variations in the sources of organic aerosol in Xi'an, Northwest China: the importance of biomass burning and secondary formation, Sci. Total Environ., 737, 139666, https://doi.org/10.1016/j.scitotenv.2020.139666, 2020.

Zhu, C. S., Cao, J. J., Hu, T. F., Shen, Z. X., Tie, X. X., Huang, H., Wang, Q. Y., Huang, R. J., Zhao, Z. Z., Mocnik, G., and Hansen, A. D. A.: Spectral dependence of aerosol light absorption at an urban and a remote site over the Tibetan Plateau, Sci. Total Environ., 590−591, 14−21, https://doi.org/10.1016/j.scitotenv.2017.03.057, 2017.